Section A-Research paper
ISSN 2063-5346

Facile synthesis of *β*-MnO_2 decorated with nitrogen doped carbon dots from expired cough syrup to enhance the dye adsorption efficiency form aqueous solution.

Klewos Synshiang[1*], Binny Mary Marwein[1], Naveen Kumar, Daneshver Kumar Verma Suja P. Devipriya'[2]

[1]Department of Ecology and Environmental Sciences, Pondicherry University, Kalapet, Pondicherry, 605014, India.

[2]School of Environmental Studies, Cochin University of Science and Technology, Kochi 682022, India.

Corresponding Author- klewossynshiang.ks@gmail.com

Abstract

Currently we present a simple technique to prepare nitrogen doped- carbon quantum dots (N-CQD) from spoiled/expired cough syrup. As prepared N-CQD was then utilised as a reducing agent to obtain nanostructured *β*-MnO_2. The physicochemical properties of N-CQD and *β*-MnO_2-CQD particles were characterised by using various techniques. The dye removal efficiency of *β*-MnO_2-CQD was studied using methylene blue (MB). The absorption results show that dye concentrations, nanocomposites dosage, pH, conductivity, and temperature affected the dye removal capacity of the β-MnO_2-CQD. The adsorption isotherm and kinetics model agreed well with Langmuir and pseudo-second order, respectively.

Keywords: Medical waste, *β*-MnO_2, N-CQD, adsorption mechanism, kinetics and isotherm.

1. Introduction

The unsustainable utility and releasing of multiple pollutants into water bodies has led to a worldwide water crisis which is a cause of concern [1]Industrial wastewater discharges poisonous and carcinogenic chemicals, destroying aquatic life and making the water unfit for domestic use. Thus, hazardous dyes from leather, paper, textile, cosmetics, rubber, and plastic should be treated before being release as most color molecules are hazardous, they are recalcitrant to environmental influences and tend to accumulate[2,3]. Textile wastewater treatment and recycling have always been feasible water scarcity solutions[4]. Adsorptions are the simplest treatment techniques they are highly efficient, economically viable and doesn't generate any secondary pollutants[5].

Expired drugs discharge into the aquatic environment are considered as emerging water pollutants [6], they are known to cause disturbing environmental and human health impacts when improperly disposed into the surrounding environment[7], with this in mind we have chosen waste cough syrup as a source for synthesis of our catalyst as its remains frequently used and seems to surge in demands in the recent years, this process will not only convert the potentially harmful material into suitable thing but serve as one of the alternative way of recycling which makes our approach green in nature.

Manganese oxide nanoparticles, which are cheap, abundant, non-toxic, and acid-resistant, have found several applications. MnO_2 as a catalyst for water treatment has found use in multiple applications, namely in adsorbent studies, cation exchange, biosensor, dye degradation and oxidation of organic matter[8,9]**.** Carbon Quantum Dots or CQD is a fast-emerging material comprising of carbon, oxygen, nitrogen and hydrogen functionalities [10]. CQD has a variety of potential utilization in sensing, bioimaging and catalysis. CQD is seen as a possible alternative to metal-based nanomaterials as a result of their exceptional photophysical qualities, tuneable emission, large surface area, low toxicity, biocompatibility, water-solubility, resistance to chemical effects and potential to act as a substrate to various desired functional groups [11,12,13]. Thus in this current study N- CQDs generated from the expired cough syrup is utilize to prepare MnO_2/CQD nanocomposite. The prepared material was then successfully applied for the removal of toxic MB dye from water solution. MB dye is hazardous to living species and damaging to aquatic ecosystems, hence its removal from various discharges is important. The method followed for the preparation of N-CQDs from waste/expired cough syrup is simple, unique as well environmentally sound in nature.

2. Experimental.

2.1 Materials.

Merk, India, supplied the potassium permanganate (KMnO4) and Methylene Blue dye. Waste/expired Ascolix cough syrup was used. Sodium Chloride (NaCl) was purchased from Fisher Scientific, India. 100 mL steel autoclave lined with Teflon was used for hydrothermal synthesis of N-CQD. The remaining chemicals reagents were of the analytical grade and utilized as obtained.

2.2 Synthesis of N-CQDs from cough syrup.

15mL of expired Ascolix cough syrup was mixed with 30mL of distilled water to synthesise N-CQDs hydrothermally. The solution was mixed and stirred for 15 minutes. The evenly mixed solution was then poured into a 100 mL Teflon-lining hydrothermal reactor and heated at 180 °C for 2.5 hrs. After the reaction the hydrothermal reactor is left to cool down to room temperature and the liquid supernatants obtained was then subjected to centrifugation and filtration. The expired Ascolix cough syrup used above consist of two medicine *Chlorpheniramine Maleate* $C_{20}H_{23}ClN_2O_4$ *and Dextromethorphan Hydrobromide* $C_{18}H_{28}BrNO_2$.

2.3 Synthesis of MnO_2CQD nanoparticles

MnO_2CQD nanoparticles was prepared similarly as reported [11], the procedure involved a simple heating method using a magnetic stirrer in which 250 mg of $KMnO_4$ was mixed with 20 mL of N-CQD solutions and stirred at 80° C for 2 h. The solution turns dark brown from pink colour at the end of the reaction producing a brown precipitate. The resulting solution is then dried in a hot air oven to obtain powdered composite. The powdered MnO_2/CQD nanocomposite was washed numerous times using excess distilled water and again dried after which it is finely crushed then used for various adsorption studies. When N-CQD was added to $KMnO_4$ solution it caused the reduction of permanganate which leads to deposition of MnO_2 on the matrix of N-CQD, as the reduction reaction of Mn^{7+} to Mn^{4+}progress the unreacted MnO_2 settled down while unreacted K_2CO_3, $KHCO_3$ and N-CQD remains as

supernatant which is then removed [1114] .In this reaction N-CQD acted both as a reducing and precipitating agent, the reduction of $KMnO_4$ to MnO by N-CQD is defined by equation[14].

$$4KMnO_4 + 3C+H_2O \longrightarrow 4KMnO + K_2CO_3+2KHCO_3 \quad (1)$$

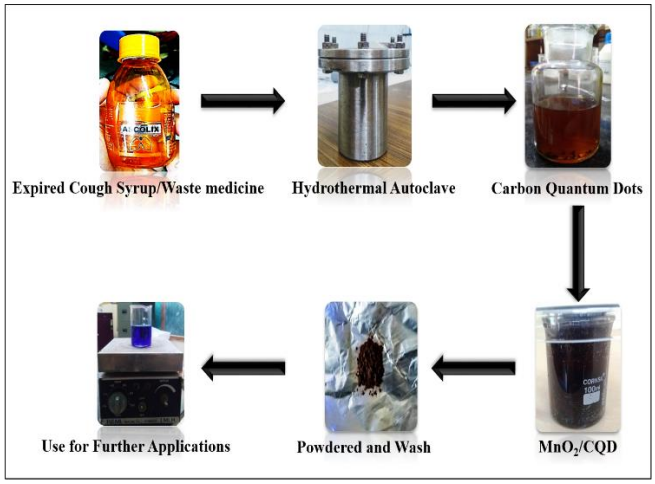

Scheme- Shows synthesis of MnO_2CQD nanocomposites.

2.4 Characterization

UV-Vis spectra were characterized using Varain 5000 spectrophotometer, while Jobin Yvon FLUOROLOG - FL3-11 was used to record the PL spectra. Thermo Nicolet 6700 with KBr method was utilized to analyse Fourier Transform Infrared (FT-IR) spectra. Raman spectrum was obtained using Horiba Jobin Vyon, LabRam. SEM images were taken using Jeol 6390LV/OXFORDXMXN**.** TEM images were acquired using Joel/JEM 2100. DLS and Zeta potential was recorded using Malvern Zeta Sizer Nano S and Litesizer 500 respectively. XRD pattern of the nanocomposite were recorded using a Cu-Kα radiation with a diffractometer Philips PW 3710/3020 and XPS spectrum was analysed using Thermo Fisher K-Alpha. The equilibrium concentration of MB dye at certain time interval was analysed using UV-Vis spectrophotometer Systronics: 119.

2.5 Adsorption studies.

The adsorptions studies were perform using 100 mL beakers in which 50 mL solution containing known amount of dye in mg L^{-1} and known dosage of MnO_2CQD in mg was taken and stirred on a magnetic stirrer, the experiments was carried out in the dark, within the first few minutes of the experiment there is a rapid change in colour from dark blue to much lighter blue indicating the adsorption of dye into the nanocomposites. After certain interval of time 2 mL of the solution was drawn out using a pipette and subjected to UV-spectrophotometer analysis. Methylene blue (MB) was taken as a representative dye. The quantity of dye removed/adsorbed and the percentage of adsorption were calculated using Eq. (2) and Eq. (3) respectively:

$$Q_e = \frac{(C_0 - C_e)V}{m} \quad (2)$$

$$\% \text{ of adsorption} = \frac{(C_0 - C_e)}{C_0} \times 100\% \quad (3)$$

Where, Q_e is the quantity of dye in mg g^{-1} adsorbed by the per unit weight of adsorbent at equilibrium. C_0 and C_e are the initial and equilibrium dye concentration in mg L^{-1}. V is the volume of the solution in millilitre (mL) and m is the weight of the adsorbent in milligrams.

3. Results and discussion.

3.1 Spectral Characterisation of MnO_2CQD nanoparticles.

The absorption spectra of pristine N-CQD, MnO_2CQD, and $KMnO_4$ solutions were taken in the wavelength range of 200-800 nm for comparison and the acquired results are shown in Fig. 1a As we can see N-CQD spectra revealed a peak at 290 nm owing to the presence of π-π* transition of the C = C bonds [11,15]**.** It is obvious from Fig. 1(a) that the absorption spectra of aqueous $KMnO_4$ solution is well characterised with peaks at 210, 310 and 350 nm ascribed to the charge transfer within the ligand oxygen, whereas the absorption peaks at 505, 524 546 and 568 nm are due to the charge transfer form ligand to metal [11]**.** When the $KMnO_4$ is heated with N-CQD solution the pink colour slowly faded and dark brown precipitate is obtained, the spectra of mixture of N-CQD and $KMnO_4$ solution shown in Fig. 1a reveal that the typical adsorption peak corresponding to $KMnO_4$ was replaced with the appearance of a wide broad peak between 200-300 nm. Moreover, the adsorption intensity of N-CQD is significantly reduced in the presence of $KMnO_4$ [16]. Steady state fluorescence spectroscopic analysis was done to confirm the formation of N-CQD from cough syrup; Fig. 1b depicts the emission spectra of N-CQD at different excitation wavelength. It is observed that changes in excitation wavelength significantly vary the intensity of emission wavelength [11,15]**,** the intensity of emission increases as the excitation wavelength increase with maximum intensity at 530 nm corresponding to the excitation at 480 nm, this emission excitation dependant nature of the N-CQD can be attribute to the presence of polydispersity or different-sized carbon dots and availability of various functional groups[17]. To further confirm the formation of CQD from cough syrup aqueous solution of N-CQD was exposed to UV light in which the brown yellowish CQD suspension showed blue fluorescence upon exposure to UV (360nm) inset in Fig. 1a (i) &(ii).

3.2 Morphology and Structural characteristic of MnO_2CQD nanoparticles

(FTIR) tests were done to determine the surface functional group of MnO_2CQD and pristine CQD. As evidence in Fig. 1(c) the FTIR spectra peaks at 3317 cm^{-1} and 3405 cm^{-1} correlate to stretching vibrations of O−H or adsorbed water in pristine N-CQD and MnO_2/CQD, respectively. At around 920 cm^{-1} the bending vibration of O-H for pristine N-CQD was likewise detected [18,19]. The peaks at around 2923 cm^{-1} and 777cm^{-1} is a result of CH stretching and bending vibrations while C-O vibrations has been found at around 1253 cm^{-1} [20] for pristine N-CQD. In the case of MnO_2/CQD the peak at 860 cm^{-1} is also attributed to C-H stretching and out of plane bending vibration[21,22]. The peak at 1655 cm^{-1} for pristine N-CQD is ascribed to C=O [23]. While the NH group is responsible for the peaks centred around 1581

cm^{-1} and 630 cm^{-1} in both MnO_2CQD and pristine N-CQD, respectively [24].The COOH group of both the MnO_2CQD and pristine N-CQD is accountable for the peak at 1408 cm^{-1}, while the peak at around 1052 cm^{-1} which is only observed in pristine N-CQD is caused by the C-OH bending [25,26]. The FTIR spectra of MnO_2CQD between 400 cm^{-1} and 700 cm^{-1} shows vibrations bands which can be ascribed to metal-oxygen vibrations [27]. According to the FTIR spectra, the presence of -OH groups in the N-CQD affirms the reducing property and the capacity to donate electrons during the formation of MnO_2CQD [28]. As depicted in Fig. 1(d) the Raman peaks at 363 cm^{-1}, 590 cm^{-1}, 748 cm^{-1} and 959 cm^{-1} correspond to MnO bending and stretching vibrations [29,30,31], the peak at 1209 cm^{-1} is ascribed to D band, the band at 1413 cm^{-1} due to C-N stretching[32], while the peak at 1553 cm^{-1} and 2670 cm^{-1} is ascribed to G band and 2D band respectively.[33,34,35]

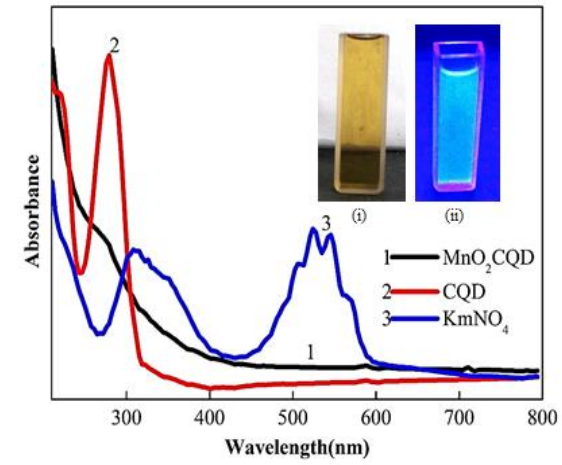

1(a)

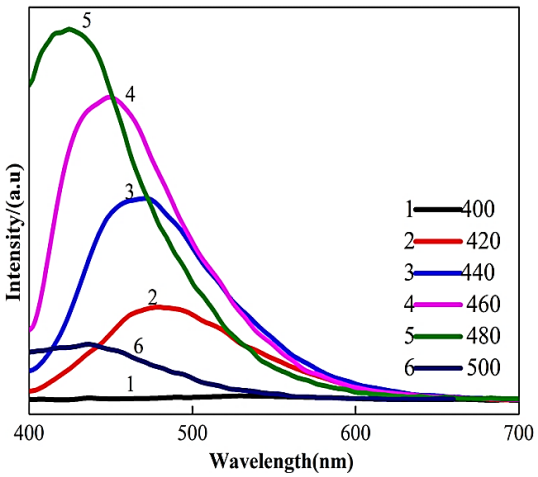

1(b)

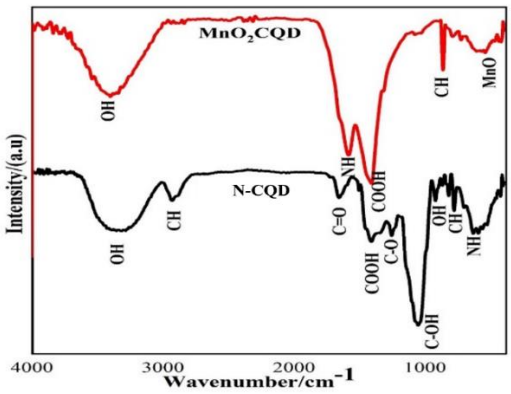

1(c)

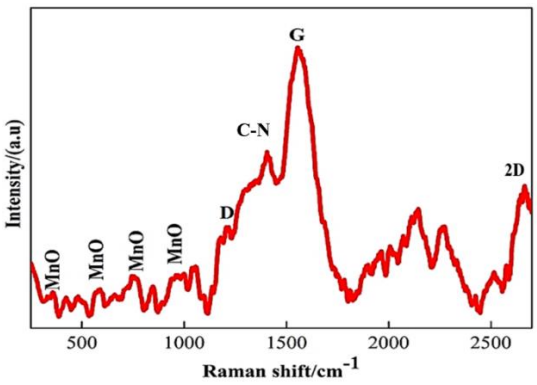

1(d)

Figure 1. (a) Adsorption spectra for pristine N-CQD, $KMnO_4$ and MnO_2CQD, inset figure (i)& (ii) shows N-CQD solution under UV light exposure (b) N-CQD emission spectra at different excitation wavelength ($\lambda_{excitation}$=400-500nm). (c) FT-IR spectrum of MnO_2CQD and Pristine N-CQD (d) Raman spectra of MnO_2CQD (e) SEM images at 10µm.

The SEM image of MnO_2CQD nanoparticles as shown in Fig. 2(a) the micrograph showed the agglomerated semi spherical grains of MnO_2CQD.TEM images of MnO_2CQD were taken

to further analyse the morphology of the MnO_2CQD. As revealed in Fig. 2(b) it was observed that the nanoparticles are composed of highly crammed semi-spherical agglomerated grains, the average size of the nanocomposite calculated from TEM images is 34.05 nm as shown in Fig. 2(c). Fig. 2(d) depicted the DLS or dynamic light scattering analysis that has been carried out to obtained the profile of nanoparticle size distribution dispersed in aqueous solution [36], DLS determine the hydrodynamic size of particles and any molecules affix to the surface, such as metabolites and solvent molecules, it is usual that the size obtained by DLS is often larger than that recorded by TEM, which may be due to Brownian motion [37] . The DLS analysis revealed a cumulative analysis with an autocorrelation function, with the generated parameters, such as the Z average and the polydispersity index or (PDI), as the primary focus [38]. The Z-average of MnO_2CQD was found to be 187.9 nm and the PDI was 0.311 at room temperature, therefore the particle size in the range below 187.9. MnO_2CQD's mean Zeta Potential was found to be -21.6 mV, thus indicating an enhanced stability of dispersion in aqueous solution at normal pH and temperature[39].

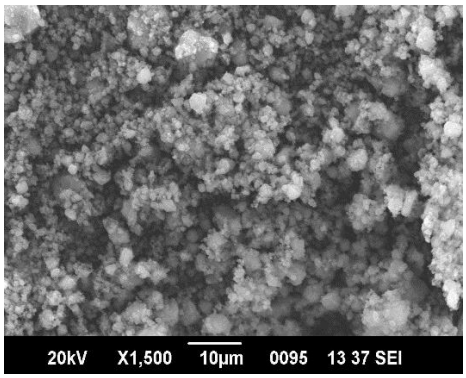

2(a)

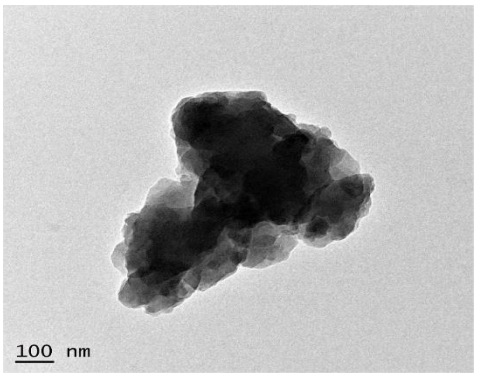

2(b)

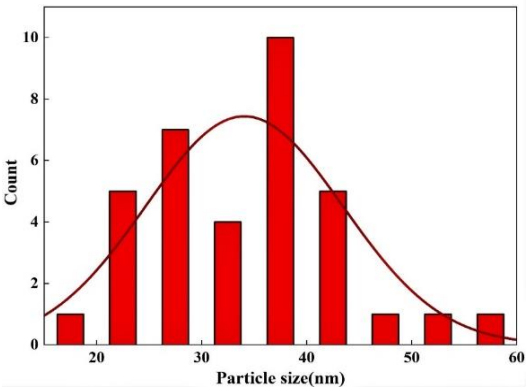

2(c)

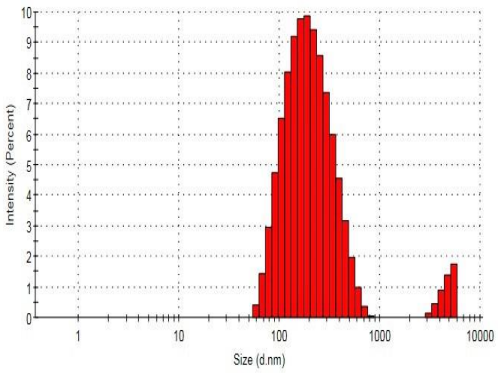

2(d)

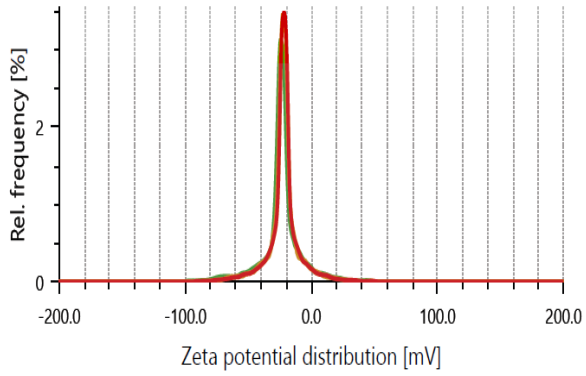

2(e)

Figure 2. (a) Show β-MnO_2CQD SEM images at 1µm (b) TEM images of β-MnO_2CQD at 100nm (c) average size of MnO_2CQD calculated form TEM images (d) & (e) accordingly depicts DLS and Zeta Potential of β-MnO_2CQD in double distilled water.

. The XRD profile of MnO_2CQD as depicted in Fig. 3(a) showed Bragg's peaks around 22.8^0, 37^0 and 48.74^0 corresponding to crystal planes of (001), (110) and (201) respectively is attributed to carbon **(AMCSD 0013020)**, whereas peaks at 32.33^0, 44.74^0,52. 19^0, 54^0.83 and 67.14^0 corresponds to diffraction crystal planes of (210) (310) (320) (321) and (420) of amorphous beta MnO_2 **(AMCSD 0009651)**.As observed, there is a shift of XRD peaks positions due to crystal structure strain which amount to defects by lattice distortion, types of strain such as tensile or compressive can shift the position of XRD peak to lower or higher angle [4041] **.** The carbon substitution in MnO lattice led to the increase of crystallite size and tensile strain since oxygen atomic radius = 0.65A is smaller as compared to the atomic radius of carbon C r = 0.77A[42]**.**

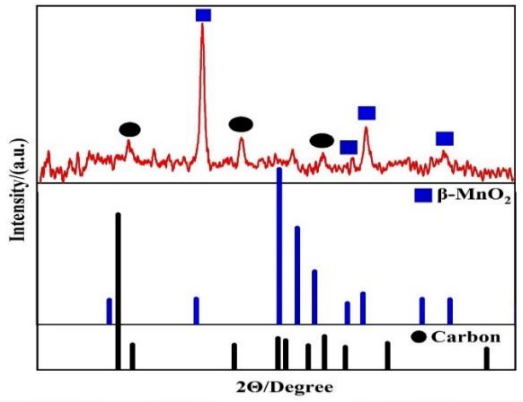

3(a)

Figure 3. (a) Shows XRD of β-MnO_2-CQD.

High resolution XPS evaluation was also performed to additional assess the chemical compositions of the prepared MnO_2CQD nano composites and as demonstrated in Fig. 4(a)

the XPS survey spectrum of the composites verified the availability of Mn, C, O, and N. The XPS spectrum of Mn 2p as depicted in the above Fig. 4(b) shows peaks at 642.9 eV attributed to $Mn2p_{3/2}$ and peaks at 653.4 eV to $Mn2p_{1/2}$. After deconvolution of the $2p_{3/2}$ and $2p_{1/2}$, Mn_2O_3 was observed at 641.9 eV and 653.4 eV while MnO_2 at 641.9 eV and 656.4 eV [43]. XPS spectrum of C 1s at 284.8eV as shown in (Figure 4 c) depicts C-C of sp^3 hybridized carbon atom[44]. The epoxy/ether C-O-C is depicted by the peaks with energy at 286.4 eV, while carboxyl O=C-O can be ascribed to peaks at 288.7 eV, 294.5 eV and 291.8 eV [45,46]. The O 1s spectrum as observed in Fig. 4 (d) shows peak with binding energy at 529.7 eV which is ascribed to the oxygen in MnO lattice without oxygen vacancy while the energy peak at 532.4 eV is related with the adsorbed oxygen, including absorbed H_2O, $–CO_3$, or O_2 [47,48]. The N s1 spectrum Fig. 4 (e) shows binding energies of pyridinic and pyrrolic nitrogen peaks at 398.8 eV and 400.7 eV, respectively[49]**,** which indicates that carbon dots are nitrogen doped **.**

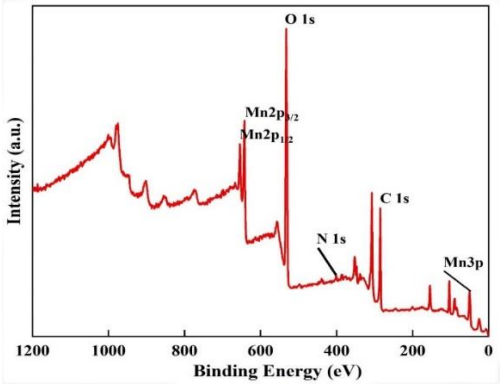

4(a)

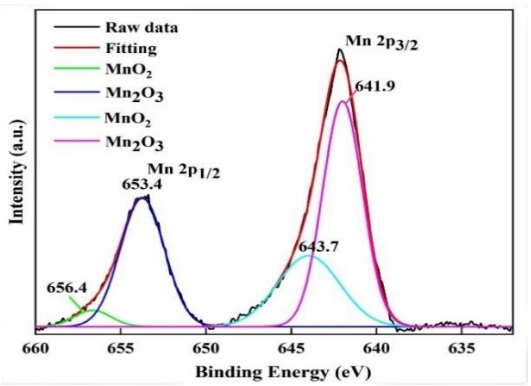

4(b)

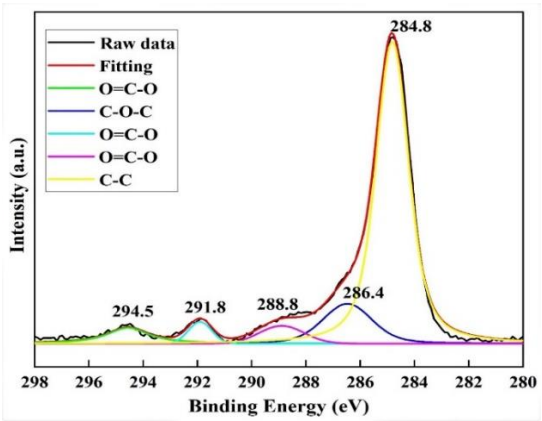

4(c)

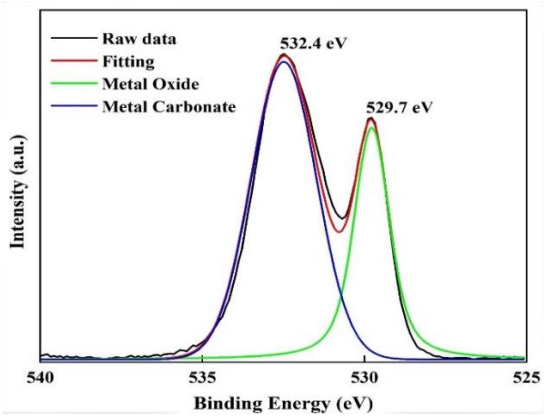

4(d)

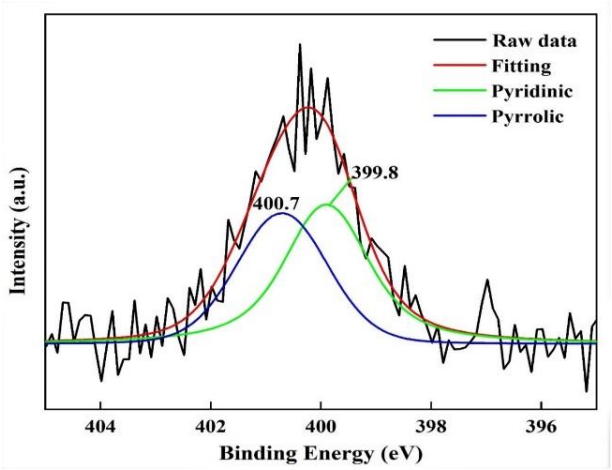

4(e)

Figure 4. (a) Shows XPS survey spectrum of MnO_2CQD (b) XPS spectrum of Mn2p (c) XPS spectrum of C 1s (d) XPS spectrum of O 1s (e) XPS spectrum of N 1s.

3.3 Optimization of the various parameters

To determine the optimal conditions for dye removal, the impact of multiple parameters such as dye amount, adsorbent quantity, duration of contact, pH, conductivity, and temperature was investigated. After optimising the various parameters the adsorption isotherm experiments was performed at 30 ℃ with various concentrations of dyes while keeping others parameters constant.

3.3.1 Effect of contact time

As demonstrated in Fig. 5(a), dye removal using β-MnO2CQD was optimized between 1-60 minutes at 5 mg L^{-1} dye concentration and 10 mg adsorbent dosage. Dye removal% was high initially but then decreased. This could be because the surface of the nanoparticles has many free absorption sites, as the adsorption process progresses, the repelling force among the dye molecules on the surface impedes adsorption on the remaining vacant sites [50]. It is apparent from Fig. 5(a) that the dye removal was quite high up to 40 minutes. As a result, for the subsequent dye removal experiments 40 minutes was fixed as the optimum time.

3.3.2 Effect of dye concentration

5 mg-25 mg L^{-1} of 50 mL MB dye concentration, contact time 40 minutes, normal pH 4.5, temperature 28℃, and adsorbent dosage of 10 mg. Depending on the initial concentration of the dye we found that the removal efficiency was found to be maximum for 5 mg L^{-1} with the removal efficiency of 97.32 % on further increasing it was found that the removal was efficient till 15 mg as shown in Fig. 5(b). The reduction in dye adsorption efficiency as dye concentration increases may be attributed to a decrease in available biding sites on the surface of MnO_2CQD. Thus, after a certain dye concentration the surface of the β-MnO_2CQD was completely covered with dye molecules preventing further adsorption and removal of dyes. As we observed that 15 mg L^{-1} of dye concentration was the most efficient with the removal efficiency of 94.68 % so 15 mg L^{-1} of dye was taken as the optimal concentration for all further investigation.

3.3.3 Effect of adsorbents concentration

To optimize adsorbent dosage 10−25 mg of β-MnO_2CQD nanoparticles, 15 mg L^{-1} of dye in 50 mL solution, normal pH-4.3, temperature 28°C and contact time of 40 min. As seen in Fig. 5(c), dye adsorption rises with adsorbent dosage, probably due to nanoparticles' many surface binding sites. Dye molecules are swiftly adsorbed, removing them quickly. Dye adsorption does not increase with adsorbent dosages above 15 mg. Thus, 15 mg of the adsorbent dosage with 96.24 % dye removal was the optimal amount for all further studies.

3.3.4 The pH effect on adsorption

The pH was optimize by varying the pH of the solution between 2-10 using 0.05 M NaOH and 0.05 M HCl while maintaining the optimized amount of dye, adsorbent concentration, temperature and time as in the preceding experiment. As shown in Fig. 5(d), at acidic pH, the amount of MB dyes adsorbed is low due to H^+, which interferes with the molecules of dye over the sites of adsorption. As pH increases, more negatively charged sites become available, increasing the binding sites for the cationic dye [51]. Therefore, pH 10 was chosen as the ideal pH for MB adsorption on MnO2/CQD.

3.3.5 The ionic effect on adsorption

The dye waste water contains more salts and metal ions[52,53,54], so the dye adsorption efficiency of the β-MnO_2CQD was tested in solutions of varying NaCl concentrations (ranging from 0-0.5 mol/L) with all parameters optimized except for temperature, which was kept at room temperature. Fig. 5(e) shows that dye adsorption decreased as ions increased. The salt curtaining the electrostatic attractions of dye molecules and particle surfaces may cause salt ions and dye molecules to compete for adsorption sites [54,55], decreasing dye adsorption with higher NaCl.

3.3.6 The effect of temperature on adsorption

The studies on the impact of temperature on the dye adsorption capability of β-MnO_2CQD nanoparticles was carried out between 30^0C to 70^0C in which a water bath containing ice were used to adjust the temperature. As shown in Fig. 5 (f), the % of dye adsorption decreases as the temperature increases from 30°C to 70°C. This is because dye adsorption in solution is an exothermic reactions [13,56] and with increase in temperature the penetration power of dye tends to reduce due to the drop in surface tension of the adsorbent [2].

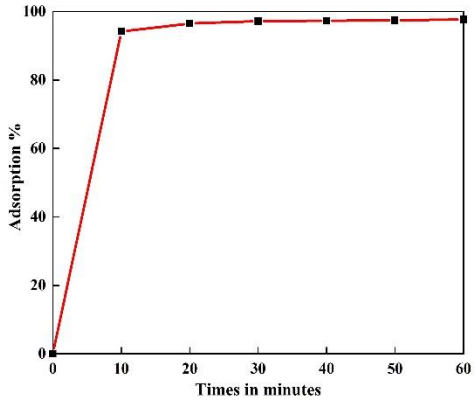

5(a)

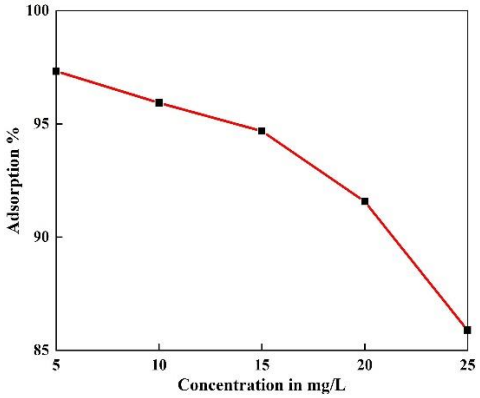

5(b)

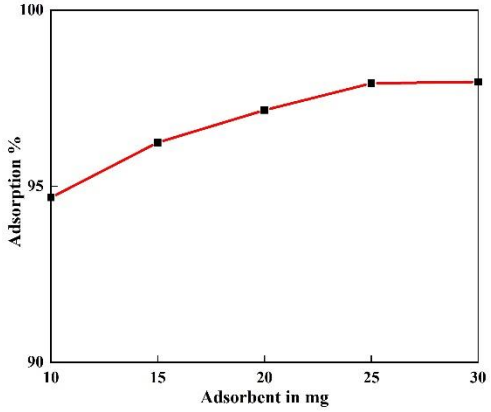

5(c)

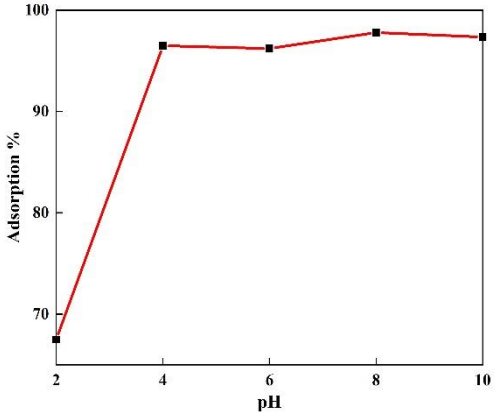

5(d)

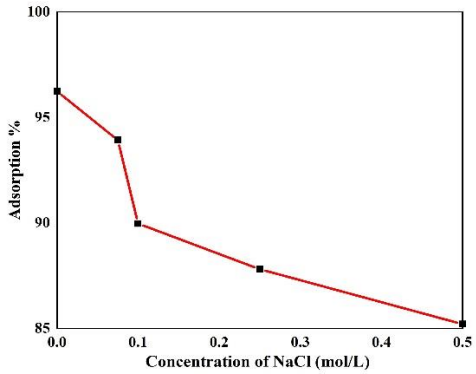

5(e)

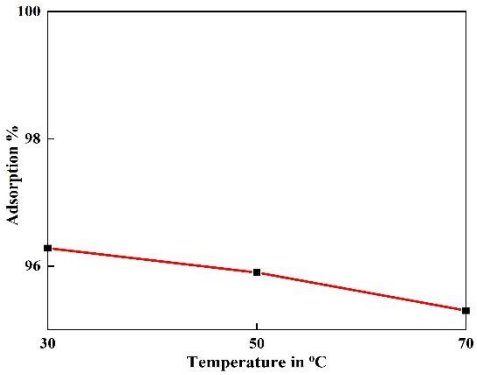

5(f)

Figure 5. (a) Effect of contact time on the adsorption% (b) effect on the adsorption % due initial concentration of dyes (c) effect on the adsorption % due to adsorbent dosage (d) effect of pH on the adsorption % (e) the effect of ionic strength on the adsorption% (f) the effect of temperature on the adsorption.

3.4 Adsorption isotherm modelling.

The adsorption isotherm or equilibrium adsorption data analysis is essential for expressing the interactive relation between the concentration of dye molecules and the amount of adsorbent in the solution to predict the adsorbent's adsorption capacity and plan the

adsorption system[57,58]. The adsorption isotherm experiment was performed at 303.15 K with the following parameters: 15 mg adsorbent, 5-20 mg L-1 dye, and normal pH were used. This study employed Langmuir equilibrium adsorption isotherm.

Langmuir adsorption isotherm is given by Eq. (4):

$$\frac{C_e}{Q_e} = \frac{1}{Q_0 L} + \frac{C_e}{Q_0} \qquad (4)$$

Where, C_e in mgL^{-1} and Q_e mgg^{-1} are the same as in Eq. (2), Q_0 is the maximum amount of adsorbate a unit mass of adsorbent can absorb, which is monolayer surface adsorption[59]. Q_0 and L were calculated using the linear regression plot of (C_e/Q_e) vs C_e in Fig. 6 (a). L is the Langmuir isotherm constant, which is related to adsorption energy [60]. R_L is provided by Eq. (5):

$$R_L = \frac{1}{1+bC_0} \qquad (5)$$

Where C_0 mg/L is the greatest starting adsorbate concentration and R_L is the type of isotherm: unfavourable if (R_L>1), linear if (R_L=1), favourable if (0<R_L<1), and irreversible if (R_L=0).Table 1 shows that R_L values favour dye adsorption into nanoparticles.

3.5 Adsorption Kinetics.

With optimum amount of adsorbate and adsorbent, a time range of 0-100 mins, pseudo second order were used to study adsorption kinetics.

The pseudo second order reaction model is given by Eq. (6):

$$\frac{t}{Q_t} = \frac{1}{h} + \frac{t}{Q_e} \qquad (6)$$

Where Q_e mgg^{-1} is same as above equation in Eq. (2), Q_t is the amount of adsorption at time *t*, *h* is the initial rate constant where $h = k_2 Q_e^2$ in which k_2 is the pseudo second order adsorption rate constant, the linear plots of $\frac{t}{Q_t}$ vs time *t* is depicted in Fig. 6 (b).

As shown, the pseudo second order can relate the whole variety of adsorption behavior[61,62] whose correlation coefficients show perfect fitness R^2 = 0.9999 of the straight line and as exhibited in Table 2 the calculated value of $Q_{e\ cal}$ is near the experimental value $Q_{e\ exp}$ making it the most suitable to study the MB adsorption process on MnO_2CQD nanoparticles.

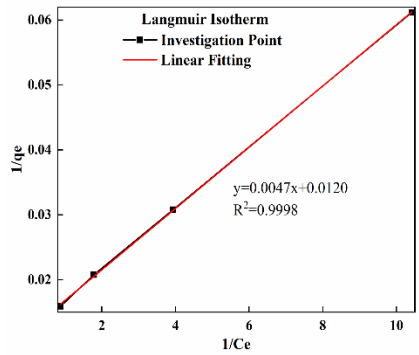

6(a)

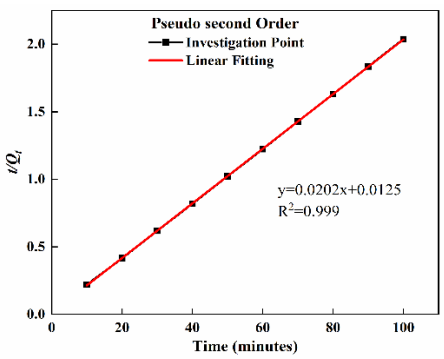

6(b)

Figure 6. (a) Langmuir adsorption isotherm and (b) Pseudo second order kinetics figures for the adsorption of MB dye on β-MnO_2CQD.

3.6 Mechanism of methylene blue adsorption

Adsorption of dyes is primarily caused by the movement of adsorbate ions to the adsorbent's outer surface, transportation of dye molecules into the adsorbent's pores, and adsorption of the adsorbate into the adsorbent's interior[63]. Multiple factors affect the overall course of adsorption such as adsorbent and adsorbate size and structures, steric effect, chemisorption, electrostatic and chemical interactions among the surface functionalities of nanoparticles and dye molecules. [64,65]. The adsorption of MB dye on to the surface of β-MnO_2CQD can be explained by the suggested mechanisms as represented by the Fig 7 (a). in which there is the Hydrogen bonding between –Oh and –COOH functional groups present on the β-MnO_2CQD and the nitrogen's atoms of MB dyes, the π–π stacking of the aromatic rings present in both β-MnO_2CQD and MB dyes, as well as the electrostatic interactions between the β-MnO_2CQD and MB dyes as evidence with the nanocomposite's large minus Zeta Potential which increases the cationic dye adsorption through electrostatic interaction, it should also be noted that the adsorption kinetics and adsorption isotherm follows pseudo second order and was consistent to Langmuir isotherm respectively similar to the one reported by [66].

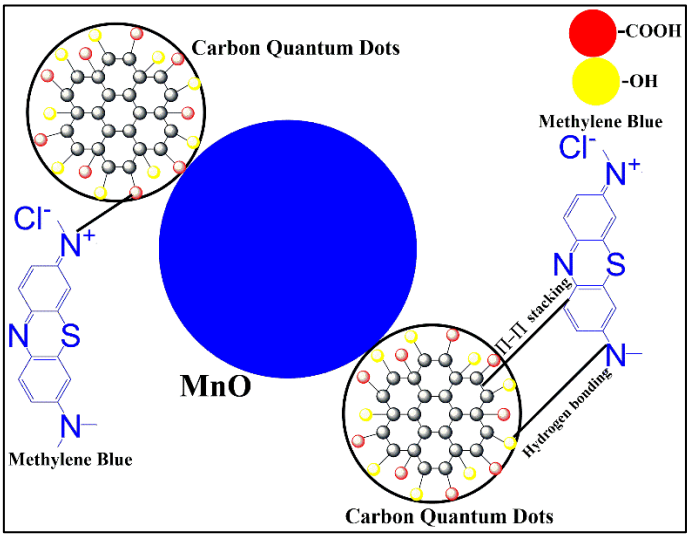

7(a)

Figure 7. (b) The adsorption mechanism of MB dye on to the β-MnO_2CQD nanoparticles similar as represented by[66].

4. Conclusion

We have demonstrated the preparation of MnO_2CQD nanoparticles, using N-CQD derived from spoiled cough syrup as a reducing agent. The obtained MnO_2CQD are quasi-spherical in shapes with the approximate size of 35 nm. It was observed that the material demonstrated rapid dye removal efficiency within a short time. The experimental adsorption and kinetics of MnO_2CQD nanoparticles fit Langmuir isotherm model with 82.85mgg^{-1} single-layer adsorption capabilities and pseudo-second-order reaction. The use of medical waste derived CQD and its metal oxide composites could be potentially used to remove dye pollutants from various solutions having wide range of pH, EC and temperature.

Tables

Table 1

Isotherm	Parameters	Value
Langmuir	Q_0 (mgg^{-1})	82.85
	R_L	0.025
	R^2	0.9998

Table 2

Kinetics	Parameters	Value
Pseudo Second Order	$Q_{e\ cal}$ (mg g^{-1})	49.45
	k_2 (g mg^{-1} min^{-1})	0.032
	R^2	0.9999

Acknowledgments

We the authors are appreciative to acknowledge the Central Instrumental Facility (CIF), Pondicherry University, Puducherry for giving us access to various instruments and facilities for characterization of our synthesised material. We are also grateful to DST-SAIF Cochin, Kerala for XRD, SEM and HRTEM analysis and Indian Institute of Technology, Guwahati, Assam for Raman characterization facility. The authors are also thankful to the Government of India for providing the necessary funds via the National Fellowship for Schedule Tribes, Id no-201718-NFST-MEG-01620.

References

1. Burket, S. R., Sapozhnikova, Y., Zheng, J. S., Chung, S. S., and Brooks, B. W., At the Intersection of Urbanization, Water, and Food Security: Determination of Select Contaminants of Emerging Concern in Mussels and Oysters from Hong Kong. 2018.
2. Shi, W., Guo, F., Wang, H., et al., Carbon dots decorated magnetic ZnFe 2 O 4 nanoparticles with enhanced adsorption capacity for the removal of dye from aqueous solution. *Appl. Surf. Sci.*, 2018, **433**, 790–797.
3. Mehra, S., Singh, M., and Chadha, P., Adverse impact of textile dyes on the aquatic environment as well as on human beings. *Toxicol. Int.*, 2021, **28**, 165–176.
4. Rosa, J. M., Fileti, A. M. F., Tambourgi, E. B., and Santana, J. C. C., Dyeing of cotton with reactive dyestuffs: The continuous reuse of textile wastewater effluent treated by Ultraviolet / Hydrogen peroxide homogeneous photocatalysis. *J. Clean. Prod.*, 2015, **90**, 60–65.
5. Hokkanen, S., Bhatnagar, A., and Sillanpää, M., A review on modification methods to cellulose-based adsorbents to improve adsorption capacity. *Water Res.*, 2016, **91**, 156–173.
6. Devi, P., Jindal, N., Kim, K. H., and Thakur, A., Nanostructures derived from expired drugs and their applications toward sensing, security ink, and bactericidal material. *Sci.*

Total Environ., 2021, **764**, 144260.

7. Shi, X., Leong, K. Y., and Ng, H. Y., Anaerobic treatment of pharmaceutical wastewater: A critical review. *Bioresour. Technol.*, 2017, **245**, 1238–1244.
8. Yang, R., Fan, Y., Ye, R., et al., MnO2-Based Materials for Environmental Applications. *Adv. Mater.*, 2021, **33**, 1–53.
9. Syed M., H., Umar, A., Azra, Y., Faisal, S., and Naseem, A., Recent trends of MnO2-derived adsorbents for water treatment: a review. *New J. Chem.*, 2020, **44**, 6096–6120.
10. Sciortino, A., Cannizzo, A., and Messina, F., Carbon Nanodots: A Review—From the Current Understanding of the Fundamental Photophysics to the Full Control of the Optical Response. *C*, 2018, **4**, 67.
11. Prasath, A., Athika, M., Duraisamy, E., Sharma, A. S., and Elumalai, P., Carbon-Quantum-Dot-Derived Nanostructured MnO2 and Its Symmetrical Supercapacitor Performances. *ChemistrySelect*, 2018, **3**, 8713–8723.
12. Mansuriya, B. D. and Altintas, Z., Carbon dots: Classification, properties, synthesis, characterization, and applications in health care-an updated review (2018–2021). *Nanomaterials*, 2021, **11**.
13. Tadesse, A., Ramadevi, D., Hagos, M., Battu, G., and Basavaiah, K., RSC Advances Synthesis of nitrogen doped carbon quantum dots / magnetite nanocomposites for e ffi cient removal of methyl blue dye pollutant from contaminated. 2018, 8528–8536.
14. Chi, H. Z., Li, Y., Xin, Y., and Qin, H., Boron-doped manganese dioxide for supercapacitors. *Chem. Commun.*, 2014, **50**, 13349–13352.
15. Wang, Y. and Hu, A., Carbon quantum dots: Synthesis, properties and applications. *J. Mater. Chem. C*, 2014, **2**, 6921–6939.
16. Jana, J., Aditya, T., Ganguly, M., and Pal, T., Carbon dot-MnO2 FRET system for fabrication of molecular logic gates. *Sensors Actuators, B Chem.*, 2017, **246**, 716–725.
17. Mathew, S., John, B. K., Thara, C. R., Korah, B. K., and Mathew, B., One-pot synthesis of sustainable carbon dots for analytical and cytotoxicity studies. *Biomass Convers. Biorefinery*, 2023.
18. Teymourinia, H., Salavati-Niasari, M., Amiri, O., and Safardoust-Hojaghan, H., Synthesis of graphene quantum dots from corn powder and their application in reduce charge recombination and increase free charge carriers. *J. Mol. Liq.*, 2017, **242**, 447–455.
19. Jain, G., Rocks, C., Maguire, P., and Mariotti, D., One-step synthesis of strongly confined, defect-free and hydroxy-terminated ZnO quantum dots. *Nanotechnology*, 2020, **31**.
20. Yang, X., Wang, Y., Xu, J., and Zhao, M. X., A multifunctional carbon dots with near-infrared fluorescence for Au3+/Hg2+ and GSH detection and tumor diagnosis. *Microchem. J.*, 2021, **165**, 106033.
21. Devi, S., Kaur, A., Sarkar, S., Vohra, S., and Tyagi, S., Synthesis and characterization of highly luminescent N-doped carbon quantum dots for metal ion sensing. *Integr.*

Ferroelectr., 2018, **186**, 32–39.

22. Singh, S., Nigam, P., Pednekar, A., Mukherjee, S., and Mishra, A., Carbon quantum dots functionalized agarose gel matrix for in solution detection of nonylphenol. *Environ. Technol. (United Kingdom)*, 2020, **41**, 322–328.

23. Kumar, A., Chowdhuri, A. R., Laha, D., Mahto, T. K., Karmakar, P., and Sahu, S. K., Green synthesis of carbon dots from Ocimum sanctum for effective fluorescent sensing of Pb2+ ions and live cell imaging. *Sensors Actuators, B Chem.*, 2017, **242**, 679–686.

24. Hu, G., Lei, B., Jiao, X., et al., Synthesis of modified carbon dots with performance of ultraviolet absorption used in sunscreen. *Opt. Express*, 2019, **27**, 7629.

25. Wang, C., Xu, Z., Cheng, H., Lin, H., Humphrey, M. G., and Zhang, C., A hydrothermal route to water-stable luminescent carbon dots as nanosensors for pH and temperature. *Carbon N. Y.*, 2015, **82**, 87–95.

26. Zulfajri, M., Gedda, G., Chang, C. J., Chang, Y. P., and Huang, G. G., Cranberry Beans Derived Carbon Dots as a Potential Fluorescence Sensor for Selective Detection of Fe3+ Ions in Aqueous Solution. *ACS Omega*, 2019, **4**, 15382–15392.

27. Van der Horst, C., Silwana, B., Iwuoha, E., and Somerset, V., Synthesis and Characterization of Bismuth-Silver Nanoparticles for Electrochemical Sensor Applications. *Anal. Lett.*, 2015, **48**, 1311–1332.

28. Alarfaj, N. A., El-Tohamy, M. F., and Oraby, H. F., CA 19-9 pancreatic tumor marker fluorescence immunosensing detection via immobilized carbon quantum dots conjugated gold nanocomposite. *Int. J. Mol. Sci.*, 2018, **19**.

29. Cetinkaya, T., Tocoglu, U., Uysal, M., Guler, M. O., and Akbulut, H., A parametric study on the rapid synthesis of one dimensional (1D) α-MnO2 nanowires. *Microelectron. Eng.*, 2014, **126**, 54–59.

30. Ede, S. R., Anantharaj, S., Nithiyanantham, U., and Kundu, S., DNA-encapsulated chain and wire-like β-MnO2 organosol for oxidative polymerization of pyrrole to polypyrrole. *Phys. Chem. Chem. Phys.*, 2015, **17**, 5474–5484.

31. Özcan, S., Güler, A., Cetinkaya, T., Guler, M. O., and Akbulut, H., Freestanding graphene/MnO2 cathodes for Li-ion batteries. *Beilstein J. Nanotechnol.*, 2017, **8**, 1932–1938.

32. Zhang, B., Xu, Y., Zheng, Y., et al., A facile synthesis of polypyrrole/carbon nanotube composites with ultrathin, uniform and thickness-tunable polypyrrole shells. *Nanoscale Res. Lett.*, 2011, **6**, 1–9.

33. Elcey, C. D. and Manoj, B., Graphitization of coal by bio-solubilization: Structure probe by Raman spectroscopy. *Asian J. Chem.*, 2016, **28**, 1557–1560.

34. Hekmat.F, Sohrabi.B, R. M., Effect of Template on the Structure of Carbon Nanotubes Grown by Catalytic Chemical Vapor Deposition Method. *Mod. Chem. Appl.*, 2017, **05**, 1–5.

35. Sole, C., Drewett, N. E., and Hardwick, L. J., Insitu Raman study of lithium-ion

intercalation into microcrystalline graphite. *Faraday Discuss.*, 2014, **172**, 223–237.

36. Saxena, A., Tripathi, R. M., and Singh, R. P., Biological synthesis of silver nanoparticles by using onion (Allium cepa) extract and their antibacterial activity. *Dig. J. Nanomater. Biostructures*, 2010, **5**, 427–432.

37. Zhang, X. F., Liu, Z. G., Shen, W., and Gurunathan, S., Silver nanoparticles: Synthesis, characterization, properties, applications, and therapeutic approaches. *Int. J. Mol. Sci.*, 2016.

38. Verma, R., Khan, A. B., Khan, M. I. K., et al., Microwave-Assisted Biosynthesis of CuO Nanoparticles Using Atalantia monophylla (L.) Leaf Extract and its Biomedical Applications. *Chem. Eng. Technol.*, 2021, **44**, 1496–1503.

39. Liao, D. L., Wu, G. S., and Liao, B. Q., Zeta potential of shape-controlled TiO2 nanoparticles with surfactants. *Colloids Surfaces A Physicochem. Eng. Asp.*, 2009, **348**, 270–275.

40. Kumari, R., Sahai, A., and Goswami, N., Effect of nitrogen doping on structural and optical properties of ZnO nanoparticles. *Prog. Nat. Sci. Mater. Int.*, 2015, **25**, 300–309.

41. Taziwa, R., Meyer, E., Katwire, D., and Ntozakhe, L., Influence of Carbon Modification on the Morphological, Structural, and Optical Properties of Zinc Oxide Nanoparticles Synthesized by Pneumatic Spray Pyrolysis Technique. *J. Nanomater.*, 2017, **2017**.

42. Wu, F., Su, H., Wang, K., Wong, W. K., and Zhu, X., Facile synthesis of N-rich carbon quantum dots from porphyrins as efficient probes for bioimaging and biosensing in living cells. *Int. J. Nanomedicine*, 2017, **12**, 7375–7391.

43. M. Tirmali, P., M. Mane, S., L. Kadam, S., and B. Kulkarni, S., Structural, electronic and magnetic investigations on PLD based La2Ni1-xFexMnO6 disordered thin films. *Adv. Mater. Lett.*, 2017, **8**, 958–964.

44. Zhang, X., Wang, S., Zhu, C., et al., Carbon-dots derived from nanodiamond: Photoluminescence tunable nanoparticles for cell imaging. *J. Colloid Interface Sci.*, 2013, **397**, 39–44.

45. Guo, C., Li, Y., Xu, Y., et al., A Highly Nanoporous Nitrogen-Doped Carbon Microfiber Derived from Bioresource as a New Kind of ORR Electrocatalyst. *Nanoscale Res. Lett.*, 2019, **14**.

46. Morais, A., Alves, J. P. C., Lima, F. A. S., Lira-Cantu, M., and Nogueira, A. F., Enhanced photovoltaic performance of inverted hybrid bulk-heterojunction solar cells using TiO 2 /reduced graphene oxide films as electron transport layers. *J. Photonics Energy*, 2015, **5**, 057408.

47. Yang, J., Yang, Z., Meng, T., Han, Y., Wang, X., and Zhang, Q., Effects of silicon doping on the performance of tin oxide thin film transistors. *Phys. Status Solidi Appl. Mater. Sci.*, 2016, **213**, 1010–1015.

48. Nayak, P. K., Wang, Z., Anjum, D. H., Hedhili, M. N., and Alshareef, H. N., Highly stable thin film transistors using multilayer channel structure. *Appl. Phys. Lett.*, 2015, **106**.

49. Artyushkova, K., Kiefer, B., Halevi, B., Knop-Gericke, A., Schlogl, R., and Atanassov, P., Density functional theory calculations of XPS binding energy shift for nitrogen-containing graphene-like structures. *Chem. Commun.*, 2013, **49**, 2539–2541.

50. Narkiewicz, U., Konicki, W., Sibera, D., Mijowska, E., and Lendzion-bielun, Z., Journal of Colloid and Interface Science Equilibrium and kinetic studies on acid dye Acid Red 88 adsorption by magnetic ZnFe 2 O 4 spinel ferrite nanoparticles. 2013, **398**, 152–160.

51. Rafatullah, M., Sulaiman, O., Hashim, R., and Ahmad, A., Adsorption of methylene blue on low-cost adsorbents: A review. *J. Hazard. Mater.*, Elsevier B.V., 2010, pp. 70–80.

52. Kushwaha, A. K., Gupta, N., and Chattopadhyaya, M. C., Removal of cationic methylene blue and malachite green dyes from aqueous solution by waste materials of Daucus carota. *J. Saudi Chem. Soc.*, 2014, **18**, 200–207.

53. Ahuja, N., Chopra, A. K., and Ansari, A. A., Removal of Colour from Aqueous Solutions by using Zero Valent Iron Nanoparticles. *IOSR J. Environ. Sci. Toxicol. Food Technol.*, 2016, **10**, 4–14.

54. Han, R., Zou, W., Yu, W., Cheng, S., Wang, Y., and Shi, J., Biosorption of methylene blue from aqueous solution by fallen phoenix tree's leaves. *J. Hazard. Mater.*, 2007, **141**, 156–162.

55. Doğan, M., Abak, H., and Alkan, M., Adsorption of methylene blue onto hazelnut shell: Kinetics, mechanism and activation parameters. *J. Hazard. Mater.*, 2009, **164**, 172–181.

56. Li, J., Ng, D. H. L., Song, P., Song, Y., and Kong, C., Bio-inspired synthesis and characterization of mesoporous ZnFe2O4 hollow fibers with enhancement of adsorption capacity for acid dye. *J. Ind. Eng. Chem.*, 2015, **23**, 290–298.

57. Salehi, R., Arami, M., Mahmoodi, N. M., Bahrami, H., and Khorramfar, S., Novel biocompatible composite (Chitosan-zinc oxide nanoparticle): Preparation, characterization and dye adsorption properties. *Colloids Surfaces B Biointerfaces*, 2010, **80**, 86–93.

58. Afkhami, A. and Moosavi, R., Adsorptive removal of Congo red, a carcinogenic textile dye, from aqueous solutions by maghemite nanoparticles. *J. Hazard. Mater.*, 2010, **174**, 398–403.

59. Kahrizi, P., Mohseni-Shahri, F. S., and Moeinpour, F., Adsorptive removal of cadmium from aqueous solutions using NiFe2O4/hydroxyapatite/graphene quantum dots as a novel nano-adsorbent. *J. Nanostructure Chem.*, 2018, **8**, 441–452.

60. Zafar, M. N., Dar, Q., Nawaz, F., Zafar, M. N., Iqbal, M., and Nazar, M. F., Effective adsorptive removal of azo dyes over spherical ZnO nanoparticles. *J. Mater. Res. Technol.*, 2019, **8**, 713–725.

61. Yeddou, N. and Bensmaili, A., Equilibrium and kinetic modelling of iron adsorption by eggshells in a batch system: effect of temperature. *Desalination*, 2007, **206**, 127–134.

62. Günay, A., Arslankaya, E., and Tosun, I., Lead removal from aqueous solution by natural and pretreated clinoptilolite: Adsorption equilibrium and kinetics. *J. Hazard. Mater.*, 2007, **146**, 362–371.

63. Gupta, V. K., Mittal, A., Krishnan, L., and Gajbe, V., Adsorption kinetics and column operations for the removal and recovery of malachite green from wastewater using bottom ash. *Sep. Purif. Technol.*, 2004, **40**, 87–96.

64. Bharathi, K. S. and Ramesh, S. T., Removal of dyes using agricultural waste as low-cost adsorbents: a review. *Appl. Water Sci.*, 2013, **3**, 773–790.

65. Zubair, M., Mu'azu, N. D., Jarrah, N., Blaisi, N. I., Aziz, H. A., and A. Al-Harthi, M., Adsorption Behavior and Mechanism of Methylene Blue, Crystal Violet, Eriochrome Black T, and Methyl Orange Dyes onto Biochar-Derived Date Palm Fronds Waste Produced at Different Pyrolysis Conditions. *Water. Air. Soil Pollut.*, 2020, **231**.

66. El-shamy, A. G., An efficient removal of methylene blue dye by adsorption onto carbon dot @ zinc peroxide embedded poly vinyl alcohol (PVA / CZnO 2) nano-composite : A novel Reusable adsorbent. *Polymer (Guildf).*, 2020, **202**, 122565.